RAL-TR-2000-052

SURFACE EXAFS – A MATHEMATICAL MODEL

J. E. Bateman
Rutherford Appleton Laboratory, Chilton, Didcot, Oxon, UK, OX11 0QX

22 November 2000

Abstract

Extended x-ray absorption fine structure (EXAFS) studies are a powerful technique for studying the chemical environment of specific atoms in a molecular or solid matrix. When applied to the study of the surfaces of thick samples it becomes necessary to measure the fluorescent products of the primary x-ray absorption cross-section. These products (fluorescent x-rays and auger electrons) must escape from the surface to be detected. This process is governed by the properties of the emitted radiation and of the material. It can easily destroy the linear relation between the detected signal and the absorption cross-section. Also affected are the probe depth within the surface (important in studies of catalytic layers) and the background superimposed on the detected emission signal. A general mathematical model of the escape processes is developed which permits the optimisation of the detection modality (x-rays or electrons) and the experimental variables to suit the composition of any given surface under study.

1. Introduction

Extended x-ray absorption fine structure analysis (EXAFS) is a useful and much used tool for the study of the environment of a specific elemental species of atom in a solid material.[1] The application of EXAFS to the study of thin films on surfaces by means of the emitted fluorescent radiations is well established, whether by means of the x-ray fluorescence [2] or the electron yield [3]. While showing greatly enhanced sensitivity for thin films and dilute samples compared to standard absorption EXAFS, the technique depends on the fluorescent products escaping from the sample surface without compromising the linearity of the detected signal against the absorption cross-section. This condition is often difficult to achieve and is dependent on the detailed properties of the surface under study. The non-linearities are generally known by the term “self-absorption” [4,5,6] and corrections are normally applied on an ad hoc basis.

Localisation of the detected signal to that from a surface film of interest is an important concern. When the atom under study is identical to (or close to in atomic number) the substrate material (e.g. a metal atom in an oxidised layer) it is difficult to resolve the EXAFS signal from the surface atoms against that from the substrate. Manipulations of the experimental conditions can significantly improve the situation [7] in the light of a model of the escape processes.

The following model for the generation and escape of the fluorescent products in surface EXAFS is aimed at providing a general formalism which can be applied to any desired sample to evaluate the expected sensitivity, delineate the limits to the linear evaluation of the absorption cross-section and estimate the background affecting the signal. It also provides a guide to methods for decreasing the probe depth and increasing the surface specificity of EXAFS measurements.

In this report the use of the term “auger” for the detected electron signal refers (unless otherwise stated) to the whole energy spectrum of emitted electrons and not to the energy-selected electrons which are often used to define an auger EXAFS spectrum [3].

2. A model for Surface EXAFS - (detecting the x-rays)

2.1 A semi-infinite slab

In figure 1 a parallel beam of N_0 x-rays per second is incident on a sample surface at a glancing angle of ϕ. In a slice of sample dx at depth x this gives rise to an isotropic source of fluorescent x-rays of rate:

$$dN = N_0 Y_i \exp\left(\frac{-\mu x}{\sin\phi}\right)\frac{\mu_i dx}{\sin\phi} \qquad (1)$$

where μ is the total absorption coefficient of the material at the x-ray energy of interest, and μ_i is the partial absorption coefficient of the i^{th} species of atom (the one under study). Let $\mu_i = F_i\mu$. In a pure element $F_i \approx 0.85$ for a wide range of K shell

edges, but in a compound sample it can be very much smaller. Y_i is the fluorescent yield of the ith atom in the shell stimulated.

The fluorescent x-ray rate *dN* is radiated into 4π. Considering the rate emitted into a conical slice $d\theta$ at an angle θ to the normal to the surface we find a fraction of $0.5d(\cos\theta)$ and this rate of x-rays experiences attenuation by the factor $\exp\left(\frac{-\mu_f x}{\cos\theta}\right)$ on the way to the surface. (μ_f is the absorption coefficient of the material at the energy of the fluorescent x-ray.) Putting all this together yields the differential expression:

$$dN = \frac{N_0 F_i \mu}{2\sin\phi}\exp\left(-\frac{\mu x}{\sin\phi}-\frac{\mu_f x}{\cos\theta}\right)dx\,d(\cos\theta) \qquad (2)$$

Integrating (2) successively over *x* (limits: 0-ω) and $\cos\theta$ (limits: 1-0) yields the rate of fluorescent x-rays which escapes from the surface to be detected:

$$N = \frac{N_0 F_i Y_i}{2}\left[1-\frac{1}{w}\ln(1+w)\right] \qquad (3)$$

where *w* is the dimensionless quantity $\frac{\mu}{\mu_f \sin\phi}$. For symmetry with the electron case this is written: $\frac{\mu\lambda_f}{\sin\phi}$ where λ_f is the attenuation length of the fluorescent x-rays in the sample. The functional dependency on *w* in expression (3) is labelled $\varepsilon_f(w)$ $\left(=\frac{1}{2}\left[1-\frac{1}{w}\ln(1+w)\right]\right)$ and it represents the efficiency with which the x-rays generated in the sample reach the surface. Figure 2 shows the behaviour of ε_f as a function of w. At low values of *w* the emitted x-ray rate is proportional to *w* (and therefore to μ, since λ_f is fixed by the x-ray line energy and sinϕ is fixed by the experimental set-up). At high values of *w*, however all possible x-rays reach the surface (i.e. 50% of those generated) and the emitted x-ray rate is independent of *w* and μ. The x-ray absorption cross-sections used in this report come from reference [8].

The usefulness of the emitted fluorescent x-ray signal is thus determined by the value of *w*. This value is partially set by the sample itself in the product $\mu\lambda_f$ (or the ratio λ_f/λ where $\lambda = 1/\mu$ - the absorption length of the incoming x-rays) and partially by sinϕ which is an experimentally variable parameter. The significance of figure 2 for various applications of surface EXAFS (x-ray fluorescence) is discussed below.

2.2 A thin film

Integrating equation (2) over the same limits in cosθ but with limits 0-d (where d is the thickness of a thin layer) results in the following relation for ε_f:

$$\varepsilon_f(b,w) = \frac{1}{2}\left\{1 - \frac{1}{w}\ln(1+w) - \int_0^1 \frac{1}{(1+\frac{1}{uw})}\exp\left[\frac{\mu d(1+\frac{1}{uw})}{\sin\phi}\right]du\right\} \quad (4)$$

Now the escape efficiency is a function of the two variables: $b = \mu d/\sin\phi$ and $w = \mu\lambda_f/\sin\phi$. Equation (4) can be written as:

$$\varepsilon_f(b,w) = \frac{1}{2}\{\varepsilon_f(\infty,w) - F(b,w)\} \quad (5)$$

The integral represented by $F(b,w)$ in equation (5) can be evaluated numerically over a range of values of b. The resulting set of curves of $\varepsilon_f(b,w)$ against w with b as parameter are shown in figure 3. The converse curves $\varepsilon_f(b,w)$ against b with w as parameter are shown in figure 4.

The asymptotic behaviour of the $\varepsilon_f(b,w)$ curves is as expected: for $b\rightarrow\omega$, $\varepsilon_f(b,w)\rightarrow\varepsilon_f(w)$ as defined in equation (3) and for $w\rightarrow\omega$, $\varepsilon_f(b,w)\rightarrow\{1 - exp(-b)\}/2$ as the layer samples the incident x-ray beam finely.

3. A model for Surface EXAFS (detecting the Auger electrons)

3.1 A semi-infinite slab

The production of auger electrons by the incident x-ray beam in the layer dx at depth x is identical to that for fluorescent x-rays with the fluorescent yield Y_i replaced by $(1-Y_i)$:

$$dN = N_0(1-Y_i)\exp\left(\frac{-\mu x}{\sin\varphi}\right)\frac{\mu_i dx}{\sin\varphi} \quad (6)$$

where all the definitions are as above.

In order to evaluate the fraction of the isotropically emitted augers which escape to the surface one requires a model for the propagation of electrons in a solid medium. At electron energies close to band energies an exponentially decaying distribution is used, however with energetic electrons (>1keV) the concept of a finite range is more useful. The data used for extrapolated electron ranges in this report come from reference [8]. As discussed elsewhere [9] the standard extrapolated range as defined in reference [8] is liable to be in considerable error for electron energies of 1keV or below in the case of high atomic number (Z>30) materials. The escape model used simply counts the electrons emitted in the cone of polar angle θ_{max} where $\cos\theta_{max} = \frac{x}{R(E_A)}$ and R is the range of the auger of energy E_A in the material (figure 1). Evaluating the solid angle of this cone shows that a fraction $\frac{1}{2}\left(1-\frac{x}{R}\right)$ of the augers will penetrate the wall. Combining this with expression (6) the differential expression for the number of augers escaping from the surface of the sample is:

$$dN = \frac{N_0 F_i (1-Y_i)}{2} \frac{\mu}{\sin\phi} \exp\left(-\frac{\mu x}{\sin\phi}\right)\left(1-\frac{x}{R}\right)dx \qquad (7)$$

Integrating (7) over x (range:0-R) gives the rate of augers detected outside the sample:

$$N = \frac{N_0 F_i (1-Y_i)}{2}\left[1-\frac{1}{u}\left(1-\exp(-u)\right)\right] \qquad (8)$$

where $u = \frac{\mu R}{\sin\phi}$. It is clear that $\varepsilon_A(u) = \frac{1}{2}\left[1-\frac{1}{u}\left(1-\exp(-u)\right)\right]$ represents the escape efficiency of the augers generated by the ith shell. The auger escape efficiency (ε_A)is plotted in figure 2 as a function of *u* where it is seen to behave in a very similar manner to the fluorescent escape efficiency (ε_F) as a function of *w*. This is not surprising considering the similarity of the processes (assigning an exponential escape model to the augers would of course make the two curves identical). The auger signal is only proportional to μ for u <0.1. Any difference in sensitivity between the two detection modalities thus lies in the very different numerical values of *u* and *w* found in practical samples.

3.2 A thin film

Equation (7) can be integrated over the range *x=0* to *x=d* where *d* is the thickness of a thin layer such that *d*<*R*. The result is:

$$\varepsilon_A(\frac{d}{R},u) = \frac{1}{2}\left\{1-\frac{1}{u}+\exp(-\frac{ud}{R})(\frac{1}{u}+\frac{d}{R}-1)\right\} \qquad (9)$$

where $u = \mu R/\sin\phi$, as before. Figure 5 shows $\varepsilon_A(d/R,u)$ as a function of *u* with *d/R* as parameter. As expected, the escape efficiency reproduces the behaviour of equation (8) with *d=R*. For small values of *d/R* (≈0.1) the range of linearity in *u* is greatly extended.

Figure 5 shows that in the linear region (u<0.2) the curves for different values of *d/R* are parallel, indicating that the ratio $\varepsilon_A(d) / \varepsilon_A(R)$ is approximately independent of *u*. Figure 6 shows the behaviour of this ratio as a function of *d/R* in the linear region.

4. A Comparison of the X-ray and Auger detection modalities.

4.1 Semi-infinite samples

(i) Linearity

Figure 2 shows that useful measurements of the incremental absorption containing the spatial information about the atom under study ($\delta\mu$) requires that either *u* or *w* (depending on the detection modality chosen) must be less than unity and preferably around 0.1. Experimental control over the value of *u* and *w* exists in the choice of the glancing angle (ϕ). The nominators of *u* and *w* are, however, determined by the

physical properties of the sample. A reasonable guide to the behaviour of the critical parameters can be obtained by plotting them as a function of atomic number (Z) for the solid elements. The elemental densities are used for $Z>10$, but for $Z<10$ a density of 1g/cm^3 is used to model the effect in organic materials.

Figure 7 shows the behaviour of $\lambda\,(1/\mu)$, λ_f and R for K shell emissions as a function of Z for elemental samples (i.e. K_α x-ray emission and KLL auger emission). And figure 8 shows the behaviour of $\mu\lambda_f$ and μR over the same range of Z. These graphs show that for all elements the value of w (choosing normal incidence to minimise the angular term) lies between roughly 4 and 20. Figure 2 shows that in this region ε_f is running well into saturation and proportionality is lost. The values of μR are, on the other hand about two orders of magnitude smaller (0.04 to 0.1) making it possible to adjust the glancing angle (ϕ) to keep the value of u around 0.1, in the proportional region.

Figure 7 shows that the physical basis of this behaviour lies in the fact that the K shell auger range (R*)* is typically two orders of magnitude less (≈0.1μm) than the K_α fluorescent escape depth (λ_f) (≈10μm). Clearly, in the case of an elemental (or of a thin oxide layer on the surface) auger detection must be used if a useful signal is to be obtained. However, in the case of a compound with a matrix of material with a mean Z much higher than that of the atom under study, λ_f can be reduced by an order of magnitude or more bringing w down towards the linear region.

Figure 9 shows the effects of the non-linearity of the escape efficiencies on a typical EXAFS spectrum. The black curve is the absorption coefficient of a thin rhodium foil as measured by absorption. The red curve is that data transformed according to equation (3) to predict the curve as measured by the emitted x-ray signal. When the absorption curve is transformed according to equation (8) to simulate that predicted for the auger electron spectrum the result is indistinguishable from the original absorption curve. Normal beam incidence is chosen (ϕ=90^o) and all the curves are peak-normalised for comparison. The familiar distortion of the x-ray signal is seen with attenuation of the EXAFS amplitude. This is understandable since w=6.0 putting the response well beyond the linear region in figure 2. The auger electron signal shows no non-linearity since u=0.04, well inside the linear region.

Unfortunately, at normal incidence with a high Z material such as rhodium (Z=45) there is a high probability of the emerging K x-rays generating photoelectrons which make the observed electron signal a composite of the electron and x-ray spectra. For low Z materials with a low fluorescent yield this effect is not significant, but in general it will degrade the electron EXAFS response. This effect is known as florescent yield (FY) total electron yield (TEY) interference.

A further distortion of the electron-derived EXAFS spectrum results from the contribution of the photoelectrons (PEs) of the x-ray absorption edge which generate an energy-dependent contribution to the EXAFS signal. This can be designated as PE interference.

(ii) Fluorescent yield – Electron yield Interference

The mathematical model makes it a simple matter to generate an estimate of the FY-TEY interference as a function of the various parameters. If equation (7) is integrated only over the interaction depth x, the result describes the fraction of fluorescent x-rays emitted from the sample surface into a cone of width $d(\cos\theta)$ at polar angle θ:

$$dN = \frac{1}{2} N_0 F_i Y_i \frac{1}{\left(1+\frac{1}{w\cos\theta}\right)} d(\cos\theta) \qquad (10)$$

Since the photoelectron range $R<<\lambda_k$, the number of L-shell derived photoelectrons produced within the escape depth (R) from the surface is just:

$$dN = \frac{1}{2} N_0 F_i Y_i \frac{1}{\left(1+\frac{1}{w\cos\theta}\right)} \frac{R}{\lambda_k} d(\cos\theta) \qquad (11)$$

Integrating equation (11) over the full range of $\cos\theta$ (1-0) gives the number of photoelectrons produced in the escape depth:

$$N = \frac{1}{2} N_0 F_i Y_i \frac{R}{\lambda_k} \ln(1+w) \qquad (12)$$

The photoelectron escape efficiency from this layer is 50% so we have, finally the number of secondary fast electrons (those produced by the K shell x-ray fluorescent x-rays):

$$N_{e2} = \frac{1}{4} N_0 F_i Y_i \frac{R}{\lambda_k} \ln(1+w) \qquad (13)$$

It will be noted that the same symbol R is retained for the range of the secondary L-shell photoelectrons as for the primary auger electrons. This is because the average energy of the two species is the same, namely the average over the sub shells of the K-shell binding energy minus twice the L-shell binding energy.

A useful measure of the interference is the ratio of the secondary electron signal to the primary auger signal as defined by equation (8):

$$F_I = \frac{N_{e2}}{N_e} = \frac{1}{4} \frac{Y_i}{(1-Y_i)_i} \frac{R}{\lambda_k} \frac{\ln(1+w)}{\varepsilon_A(u)} \qquad (14)$$

Evaluating F_I for the rhodium sample in figure 9 (Y_i=0.82, w=6.0, u=0.039, R=0.51μm, λ_k=77.7μm) gives F_I=1.88. This means that the measured electron EXAFS spectrum in figure 9 will be almost as distorted as the x-ray spectrum the secondary electron image of which dominates the primary electron signal.

Equation (14) shows that the x-ray-induced component increases only logarithmically with w while $u<<1$. This indicates that decreasing the glancing angle ϕ will increase the primary electron signal relative to the secondary one. Thus at $\phi=3^o$ (w=115.4, u=0.75) F_I=0.3. This still gives some distortion but much less than at $\phi=90^o$, while u is just out of the linear region but ε_A is not seriously saturated.

The behaviour of F_I with atomic number is governed by the fluorescent yield Y_i in equation (14). At lower atomic numbers the interference eases considerably. Thus for a nickel surface (K emission) with $\phi=3^o$ F_I=0.0078 with u=1.06. Since in the K-shell $Y_i \rightarrow 1$ for $Z>50$, it is clear that the electron EXAFS signal from an elemental sample will essentially reproduce the x-ray signal. This effect can be countered by using the L edge of high Z samples.

In a similar way as was noted for the linearity of the x-ray signal, the measurement of the electron signal from a low Z atom in a high Z matrix will be relatively uncorrupted because the beam energy will not be capable of stimulating the K shell of the matrix atoms. The interference of lower energy shells of the high Z component can be estimated by substituting the appropriate L-shell parameters in equation (14).

(iii) PE Interference

Every x-ray interaction with the atomic level under study generates a photoelectron, the energy of which is the difference between the beam energy (E_B) and the absorption edge energy (E_E). The model predicts that these electrons will escape from the surface, giving a signal:

$$N = N_0 F_i \varepsilon_{PE}(u_{PE}) \qquad (15)$$

where ε_{PE} has the same functional form as ε_A and $u_{PE} = \mu R_{PE} / \sin\phi$. Assuming that the range of the electrons in the material follows a power law, it is possible to write $R_{PE} = a(E_B - E_E)^n$ where $1<n<2$. In order to simplify the analysis it is assumed that (as is generally the case) the electron signal is in the linear region of u. Then, figure 2 shows: $\varepsilon = u / 4$. Substituting this condition into equations (8) and (15) the ratio of the PE interference signal to the auger signal is shown to be:

$$\frac{N_{PE}}{N_A} = \frac{R_{PE}}{(1-Y_i)R_A} = \frac{1}{(1-Y_i)}\left(\frac{E_B - E_E}{E_A}\right)^n \qquad (16)$$

The energy dependence of this function arises from the dependence of the escape efficiency of the PE on its energy. E_A is the energy of the corresponding auger electron.

Using the power law appropriate to the extrapolated electron range data [11] gives n = 1.22. Figure 10 shows the PE interference fraction as a function of $E_B - E_E$, as predicted by equation (16) for samples of the elements C, Ne, S, Ni and Rh. The effect of the interference is to amplify the EXAFS signal differentially throughout the scan energy range with a maximum contribution of a few percent for medium to high Z samples. For low Z samples the effect becomes very strong and the distortion of the

EXAFS signal becomes severe. There is strong evidence that the extrapolated electron range is not the correct parameter to insert into the model [9] and that the value of the range-energy index n should be ≈1.6 for medium to high Z materials. This makes the curves in figure 10 somewhat steeper while decreasing the absolute magnitude of the effect for high Z materials.

The effect on the measurement of the PE interference signal quantified in figure 10 depends very much on the method used to acquire the electron yield signal. If the sample current (TEY) is used then the effect is as predicted by figure 10 since all electrons contribute equally to the signal. If, on the other hand, an electron energy analyser is used with a threshold above the maximum value of $E_B - E_E$ the PEs will not reach the detector and auger signal will be completely clean. In a gas counter the detected pulse sums the energies of both electrons so only one count is registered for a PE + auger event and if the energy threshold is high enough no PE-only events will be recorded. Thus again, the auger spectrum is uncorrupted.

(iv) Sensitivity

Defining the sensitivity as the fraction of the beam which is converted into fluorescent products which escape the surface one obtains for the x-rays, from equation (3):

$$S_f = \frac{N}{N_0} = \frac{1}{2} F_i Y_i \varepsilon_f(w) \qquad (17)$$

and for the primary electrons:

$$S_A = \frac{N}{N_0} = \frac{1}{2} F_i (1 - Y_i) \varepsilon_A(u) \qquad (18)$$

The first determinant is clearly the fluorescent yield Y_i which, for the K shell, increases from ≈0 at Z=6 to ≈0.95 at Z=80. Thus the electron signal is favoured at low Z and the x-ray signal at high Z.

Figure 8 shows how $w(\phi=90^o) = \mu\lambda_f$ and $u(\phi=90^o) = \mu R$ vary for elemental samples over the range $6 < Z < 50$. Inserting these values into the escape efficiency functions (figure 2) shows that since $w >> 1$ the x-ray signal is generally saturated with $\varepsilon_f \approx 0.5$ while ε_A is in the linear range. Thus the approximate relations:

$$S_f \cong \frac{1}{4} F_i Y_i \qquad (19)$$

$$S_A \cong \frac{1}{4} F_i (1 - Y_i) u \qquad (20)$$

Taking a Z value such that Y_i=0.5 (the transition elements) for the purposes of comparison, one sees that ≈10% of the incident beam is converted into x-rays (F_i≈0.8) and ≈0.4% is converted into electrons. Thus the x-ray signal is copious but highly non-linear (w=5 in figure 2) while the primary electron signal is linear but much weaker. In this region of Z the corruption of the primary electron signal by the x-ray-

induced secondaries will be of the order of a few percent of the electron signal and so almost negligible (see above).

The apparent disadvantage of the electron signal is somewhat reduced when one considers the methods by which the fluorescent products are detected. In general it is difficult to cover more than 20% of 2π with an x-ray detector and window and efficiency losses can (depending on the x-ray energy) reach 50%. The result is that the practical x-ray counting rate will be ≈1% of the beam rate. Electrons can, on the other hand, be detected with 100% efficiency either by measuring the sample current or using internal counting in a gas counter. The resulting rates thus become comparable. In the electron case, one has the further option of decreasing ϕ until the edge of the linear region is reached. This increases u and therefore ε_A.

Since x-ray detectors can only (in general) view a small proportion of the emitted hemisphere, it is useful to consider the sensitivity per unit solid angle as a function of the polar angle θ. Equation (10) gives the emitted x-ray rate in cone $d(\cos\theta)$ at angle θ. This equation can be very simply converted into the counts per unit solid angle at a polar angle θ:

$$\frac{dN}{d\Omega} = \frac{1}{4\pi} N_0 F_i Y_i \frac{1}{\left(1+\frac{1}{w\cos\theta}\right)} \quad \text{sr}^{-1} \quad (21)$$

Defining the x-ray emission efficiency per steradian as $\varepsilon_{f\Omega}(\cos\theta)$:

$$\varepsilon_{f\Omega} = \frac{1}{4\pi}\frac{1}{\left(1+\frac{1}{w\cos\theta}\right)} \quad \text{sr}^{-1} \quad (22)$$

Figure 11 shows the behaviour of $\varepsilon_{f\Omega}$ as a function of w with $\cos\theta$ as parameter. Some limiting cases are interesting. With the x-ray detector at normal viewing ($\cos\theta=1$) the function saturates in the familiar manner with an asymptotic value of $1/4\pi$ (as expected). When one goes towards $\cos\theta=0$ (with the azimuthal angle set to 90^o to the beam to avoid the beam scatter) $\varepsilon_{f\Omega} \rightarrow w\cos\theta/4\pi$. This means that even with $w>1$ one can achieve a linearised EXAFS response from the x-ray signal at a corresponding sacrifice of sensitivity.

The precision of measurement of the absorption coefficient μ in a measurement of the fluorescent products is ultimately set by the Poisson statistics of the detected x-ray or electron counts. The model permits an analysis of the effect of the saturation of the x-ray and electron signals (figure 2) on the measurement precision. The standard deviation (SD) of the detected signal in T seconds of counting is $\sigma_N=(NT)^{1/2}$, where $N=N_0\varepsilon(u)$. $\varepsilon(u)$ stands for either $\varepsilon_f(w)$ or $\varepsilon_A(u)$ and the terms F_i, Y_i, $(1-Y_i)$ and any detector inefficiency are all subsumed in N_0 (as appropriate)for the present analysis.

Using the slope of the $\varepsilon(u)$ curves to convert the error in N (ε) into the corresponding error in u, and using the fact that μ is proportional to u gives:

$$\frac{\sigma_\mu}{\mu} = \frac{\sigma_u}{u} = \frac{1}{\sqrt{N_0 T}} \frac{\varepsilon^{1/2}}{\frac{d\varepsilon}{du}} \frac{1}{u} \qquad (23)$$

in terms of the beam rate. Expressing equation (23) in terms of the counting rate gives:

$$\frac{\sigma_\mu}{\mu} = \frac{\sigma_u}{u} = \frac{1}{\sqrt{N\ T}} \frac{\varepsilon}{\frac{d\varepsilon}{du}} \frac{1}{u} \qquad (24)$$

Both these equations predict the statistical precision in the absorption coefficient in terms of a multiplier to the standard statistical precision. Equation (23) gives the precision in terms of the input beam counts N_0T (remembering that the omitted factors, F_i, Y_i, etc must be reinserted for any given case). Figure 12 shows the multiplier as a function of w (x-rays) and u (electrons). As u (w) increase the error multipliers decrease to a minimum at $u = w \approx 1$ as the escape efficiency increases but increase rapidly as the escape efficiency curves move into saturation. Thus equation (21) predicts that the optimum operating point from the point of view of minimising the exposure time is at $u = w \approx 1$. Since both the x-ray and electron signals are in the non-linear region at this point corrections will be necessary.

Figure 13 shows the error multiplier (equation (24)) for the statistical error in the detected counts NT. As expected this is unity in the linear region ($u = w < 0.1$) and increases steadily as the escape efficiency curves (figure 2) move into saturation.

In the case of the EXAFS amplitude, which is a modulation $\delta\mu$ of the basic absorption coefficient, the relative SD error in $\delta\mu$ is $\sigma_{\delta\mu}/\delta\mu = \mu\sigma_\mu/\delta\mu$.

(v) Probe Depth

The depth of the sample surface stimulated by the incident beam is $\lambda sin\phi$. The escape depth is λ_f for x-rays and R for augers. In elemental samples $\lambda_f > \lambda$ and in most compounds $\lambda_f \approx \lambda$ so that one can take the probe depth as λ. On the other hand $R << \lambda$ and therefore it determines the probe depth of the beam. The escape efficiency of the auger signal can be enhanced by decreasing φ and concentrating the beam interaction in a shallower depth of surface. As discussed above one can often increase u by this means by a factor of up to 20 ($\phi \approx 3^o$), (depending on the sample) without getting into the seriously non-linear region of $\varepsilon_A(u)$. This would (typically) reduce the beam interaction depth to ≈0.5μm, i.e. comparable to the electron escape depth but not (in general) inferior. This option is not available with the x-ray signal because at the w values involved it is totally saturated.

Using the data in figure 7 it is possible to summarise this behaviour by the statement that x-ray detection will sample to a depth of ≈5μm while electron detection will sample to a depth of ≈0.25μm (sample-dependent). Modelling the escape process of the auger electrons in detail shows that as noted in reference [3] there is a further option to reduce the sampling depth when the energy of the escaping electrons is detected.

If the sample is mounted in a detector with a proportional energy response (e.g. a gas microstrip detector [7]) the detector records the residual energy of each escaping electron. Figure 14 shows the energy spectrum of residual energies of augers (KLL) from a nickel surface predicted by a simple montecarlo model of the escape process. Since the residual energy is correlated inversely with the depth of origin, selecting only the highest energies in this spectrum restricts the probe depth. The Monte Carlo model allows one to generate a histogram of the origin depth of the escaping electrons selected on the basis of their residual energies as measured in the gas detector. Figure 15 shows the depth distributions for a range of lower threshold discriminator levels (LLD) applied to the pulse height distribution in the detector. As the LLD is raised the electrons originating deeper in the surface are rejected and with the LLD set at 80% of the auger energy, the signal is effectively biased to a depth of ≈20nm, much lower than the electron range (≈170nm). Conversely, by selecting only the smallest pulses (less than 20% of the auger energy) one can bias the probe depth to a deeper level in the sample (figure 16). This possibility was demonstrated in reference [7] in which the EXAFS signal from a thin layer of nickel oxide was enhanced sufficiently to be detected successfully in the presence of the bulk nickel signal. In the practical situation the very bottom of the energy spectrum is dominated by low energy secondaries and L augers and is biased off.

The simplified model of electron escape used in this work predicts a linearly decreasing escape probability with depth from 0.5 at the surface to zero at $x=R$.The detailed physical model of Schroeder [10] shows that the true shape of this curve (over a wide range of materials in the keV energy range) is a quasi-negative exponential curve decreasing from ≈0.75 at $x=0$ to zero at $x=R$. This means that the biasing of the energy distribution according to depth is rather stronger than the model predicts. The integral of the Schroeder escape probability curve is very close to that of the linear model, which explains why the escape efficiencies generated by the simple model are found to be reliable.

The electron energy selection technique does not help with the FY-TEY interference problem since the x-ray-induced secondaries have an identical energy spectrum to the primary augers. Thus this approach will be less successful for high Z ($Z\geq 40$) elemental samples in which the interference is significant.

(vi) Background

Having ensured that the active volume of the detector can only register x-rays or fast electrons originating in the beam footprint on the sample, one can estimate the background in the EXAFS signal generated by the sample. In the case of x-ray detection the coherent scatter is (for Fe) 0.43% of the photoelectric cross-section and the incoherent scatter is 0.017%. The coherent scatter propagates in the beam direction, which with (for example) a glancing angle (ϕ) of 45^{o} can be made to entirely miss the detector. If one treats the incoherent scattering as isotropic then the ratio of the background to the K_{α} flux is just the ratio of the cross-sections divided by the fluorescent yield. For Fe this evaluates to ≈0.05%. Both forms of scattering show negligible energy shift so the photons have essentially the beam energy. If the detector has adequate energy resolution then a further reduction by energy discrimination is possible and it is in principle possible to have a background-free signal.

In the case of no energy discrimination in the detector, the background from other stimulated absorption edges can be estimated by means of equation (3) for each edge in turn by substituting the appropriate parameters.

In the auger electron case a background signal is unavoidable. Photoelectrons from inferior atomic shells (and the lower shells of any other atomic species in the sample) will always be present. Thus in the region of Fe about 15% of all interactions will generate L shell photoelectrons. Figure 14 shows the typical relation of the photoelectron and auger energy spectra (from nickel) in a proportional counter. Even with energy discrimination they cannot be separated since the photoelectron endpoint energy is higher than that of the auger for the same atom. The effect of this is to add a significant pedestal to any EXAFS spectrum. Since the L and K shell cross-sections decay with approximately the same energy dependence the pedestal remains a constant fraction of the signal throughout the scan. Since it can be applied equally to the photoelectrons as well as to the auger electrons, the model can be used to provide an estimate of the magnitude of the background. In the case of the K edge of a nickel sample the photoelectron background rate (N_{pe}) from the L,M shells relative to the primary auger signal (N_A) is found to be (using equation (8)):

$$\frac{N_{pe}}{N_A} = \frac{(1-F_i)}{F_i}\frac{1}{(1-Y_i)}\frac{R_{pe}}{R_A} \qquad (25)$$

Where F_i is the fraction of the total cross-section in the K shell interaction, Y_i is the K shell fluorescent yield, R_{pe} is the range of the L shell photoelectrons and R_A is the range of the K shell augers. In deriving equation (25) it has been assumed that the operating parameters put u in the linear region (u<0.1). Inserting the parameters for the nickel K edge: F_i=0.85, Y_i=0.42 and R_{pe}/R_A = 1.15 gives $N_{pe} = 0.35N_A$. In other words there is a very substantial pedestal which implies increased counting times to compensate for the low signal to noise ratio. The same method can be applied to the estimation of the photoelectron background from all the accessible edges in a compound sample by estimating the contribution of each edge separately and then adding them all together.

A further possible source of contamination of the signal arises in the case of auger detection in a gas counter. Since the sample must be within the counter volume the beam itself must pass through the gas and generate a background signal with pulse heights characteristic of the beam energy. This effect is minimised by adjusting the gas mixture in the counter to have as low an x-ray stopping power as possible while stopping the augers from the sample. For example a mixture of 10% isobutane in helium was used in reference [7]. The energy gap between the KLL augers and the full beam energy provides a further opportunity to reject beam breakthrough; however, this was found to be unnecessary.

(vii) Correction

As has been demonstrated in reference [4] it is in principle possible to correct the non-linearity exhibited by the surface EXAFS signal when w or u >0.1. The model provides a particularly simple option for correction. From equation (3) (the x-ray case) one can write the detected rate as:

$$N = C\varepsilon_f(w) \qquad (26)$$

where C is a constant for a given absorption edge and experimental set-up and $w = \mu\lambda_f/\sin\phi$. If the beam energy scan is continued beyond the point at which the EXAFS signal dies out the value of μ may be estimated from the known stoichiometry of the sample and tabulated absorption coefficient values. λ_f is similarly available from tables and ϕ is an experimental parameter. Thus from figure 2 the value of C can be determined and the working range of w established. Now each value of N may be converted into the corresponding value of ε_f, and through figure 2, the corresponding μ value. If a reasonable sequence of data can be accumulated in the energy region beyond the EXAFS signal (>20 points), a plot of N versus the tabular value of μ will permit a fit to be made using the functional form of $\varepsilon_f(w)$ to the two unknown parameters in equation (26), i.e. C and $\lambda_f/\sin\phi$. The correction process becomes very "ill-conditioned" if w >5 and should not be attempted in this region.

The same process may be applied to the correction of the auger signal using the relevant function (equation (8)) and $u = \mu R/\sin\phi$. However, as discussed in detail in reference [9], the tabulated values of the extrapolated range are not trustworthy for use in the model except for very low Z materials. Thus the fitting method outlined above for the x-ray signal is the only satisfactory approach to correcting the linearity. Fortunately, it is relatively easy to maintain u in the linear region for K shell edges. When transition element L shell edges are used for surface EXAFS studies, the very high values of μ at the absorption edge can push u into the non-linear region and correction is required [12].

4.2 Thin surface layers

In planning EXAFS measurements on layers of nanometer thickness two distinct problems arise; (a) obtaining a statistically significant signal from the layer and (b) avoiding this signal being drowned by emissions from the substrate. The models permit the exploration of these problems and can direct the design of the experiment.

(i) Linearity and Sensitivity

As figure 4 shows, when the x-ray emission is used and w>>1 the x-ray yield from the surface of a thin film is:

$$N = \frac{N_0 F_i Y_i}{2}\left(1 - \exp\left(\frac{-\mu d}{\sin\phi}\right)\right) \qquad (27)$$

This function is reasonably linear in μ for $b = \mu d/\sin\phi < 0.1$. This means that the linearity is not determined by λ_f but by the film thickness d. Considering K shell emissions in the region of the transition elements in figure 7, it is clear that for a layer of thickness 20nm in a material with λ=5μm, $b = 0.004/\sin\phi$. The low sensitivity implied by this value of μd can be retrieved to a large extent by using a small glancing angle such as ϕ=2°. In this case a factor of 29 increase in the signal can be obtained while b=0.115, still essentially linear in μ. Evaluating equation (27) for typical values

for Z=26 one obtains a sensitivity of 1.9%N_0 into 2π, or ≈0.19% into a typical x-ray detector. Thus for thin layers x-ray detection can yield adequate sensitivity with proportionality in μ by using small beam glancing angles.

In the case of electron detection, figure 5 shows that for d/R = 0.1 the detected rate is linear with u ($\mu R/\sin\phi$) up to the region of u=1. In the case of the nickel sample considered (KLL augers) this corresponds to a layer thickness of ≈15nm. In this situation (u=1) $\phi = 1.7^o$ and figure 6 shows that $N \approx N_0 F_i(1-Y_i)0.2u/4$. Evaluating this with the parameters used for the x-rays gives a sensitivity of 2.5%N_0. In this case the whole electron signal will in general be detected.

The model thus shows that for thin layers, the domain of linearity is considerably extended making small glancing angles practical and making the detection of thicknesses in the region of a few nanometers practicable from the point of view of sensitivity.

(ii) Background

In both the x-ray and electron cases described above ≈90% of the incident beam passes through the surface layer and generates very large backgrounds of both x-rays and electrons in the substrate. Since the surface layer is thin enough to allow essentially all the fluorescence created in the substrate to escape, the background of any particular fluorescent product (x-rays from accessible shells, augers, photoelectrons) may be calculated using the formulae for a semi-infinite slab (equations (3) and (8)).

If the detector has no energy discrimination then it is clear that signal to background ratios (S_B) of ≈0.1 are inevitable. If the substrate material has a different atomic number from the target atom in the surface layer and an energy-sensitive x-ray detector is used, then it is possible to reject the substrate background. Figure 17 shows the simulated x-ray pulse height predicted by the model in a gas microstrip detector (GMSD) when a 4nm thick layer of zinc on an iron substrate is irradiated at the zinc K edge at a glancing angle of 1^o. In spite of an intrinsic signal to background ratio of 0.06 against the iron lines, the energy resolution of the detector is sufficient to permit a discriminator level to be set which gives S_B = 12.5 with a loss of only 5% of the zinc signal.

In the case of the electron signal, no such clear discrimination of the zinc signal is possible. Figure 18 shows the electron energy spectra derived from the Monte Carlo version of the model for the same zinc-on-iron sample. Because the escape electron energy spectra extend over most of the energy range there is little discrimination possible between the electrons from the iron and those from the zinc. The model shows that at small angles of incidence the electron escape spectrum begins to peak close to the KLL auger energy. Figure 18 shows that if an energy window of 6.5keV to 7.5keV is applied the signal to background may be optimised at S_B = 0.197, a value still very poor compared to that possible with energy selection on the x-ray spectrum.

When the target atom in the layer is the same species as that of the bulk material, e.g. nickel in an oxidised layer on a nickel surface, no simple discrimination is possible and one must use the electron signal combined with energy selection of the escape

electrons as described in section 4.1(iv) above. This physically restricts the probe depth in a way impossible with the x-ray emission. Although S_B is < 1 for such measurements, experiment has shown that 65% of the EXAFS signal recorded could be attributed to the 20nm thick nickel oxide layer grown on a nickel surface, and 35% to the underlying nickel [7].

5. Discussion

Mathematical models have been developed for the escape efficiency of fluorescent products from the surface of solid samples. These are characterised by universal functions (one for x-ray emissions and one for electron emissions) which can be applied to any fluorescent emission by means of dimensionless parameters which are specified by the key parameters of the fluorescent product under consideration. These are respectively λ_f the attenuation length of an emission line in the material, and R the range of the fluorescent electron under consideration. The efficiency functions permit a detailed assessment of the many complex issues surrounding the design of surface EXAFS measurement, such as sensitivity, linearity and background. Examples have been given of how the model may be applied to quantify the various issues including such effects as FY-TEY interference in electron yield EXAFS. A number of general conclusions regarding the application of surface EXAFS emerge from the analyses performed which are worth summarising:

- Saturation of the escape efficiency as a function of the absorption coefficient μ is an almost inevitable accompaniment of the measurement of EXAFS from a semi-infinite solid surface using the fluorescent x-rays. The angle of beam incidence should be maintained near normal and corrections must be applied if true EXAFS amplitudes are to be measured. With electron yield, saturation is easily avoided and the angle of incidence can be used to control the sensitivity.

- The conversion of x-rays into fluorescent products on a surface is, in general, a fairly efficient process. If counting detectors are used one can expect rates of a few percent of the incident beam to be recorded in either x-ray yield or electron yield in the region of a K shell edge. In terms of conversion efficiency the *Z*-dependence of the fluorescent yield favours electron emission for low *Z* and x-ray emission for high *Z* atoms.

- Because it is easy to detect all the emitted electrons, the counting statistics in electron yield studies tend to be automatically higher than the x-ray statistics by an order of magnitude (depending, of course, on the fluorescent yield of the atom). However, the presence of photoelectrons from lower shells and matrix atoms produces a much higher level of background which is impossible to discriminate against fully. The poor signal to background ratio means that longer counting periods are required in order to compensate.

- The x-ray yield signal samples the surface to a depth of (typically) several microns while the electron yield samples to a depth of a few hundred nanometers (depending on *Z*). If the escape electron energy is measured, the effective sampling depth of the electron signal can be reduced to ≈20nm.

- FY-TEY interference is a very significant effect for materials with high atomic number. The electron yield signal tends to become a facsimile of the x-ray signal for $Z>45$, thus removing the surface discrimination of the electron signal. In some circumstances the interference of the x-ray signal can be reduced by using a small beam glancing angle.

- The signal distortion caused by PE interference is a serious problem for materials with $Z<15$ when the TEY signal is used (as for example from the sample current). However, using a suitable energy threshold in a detector sensitive to the electron energy completely removes the problem.

- For thin layer samples, the rules concerning linearity are modified. In particular, if the layer is very thin (tens of nm) the x-ray signal remains linear even at small beam glancing angles so that sensitivities of $\approx 0.1\%$ of the beam rate are possible for an atom in the layer. The electron sensitivity can be ten times higher but the electron signal does not offer the option of the x-ray lines for discrimination (in an energy sensitive detector) against the ten to twenty times higher background signal from the substrate. If possible the choice of substrate must be used to minimise the background signal by avoiding edges near the shell edge being studied.

In the literature the non-linearity exhibited by the x-ray fluorescent escape signal is routinely referred to as the "self absorption" effect. The model makes clear that this is a singular misnomer. The saturation of the escape efficiency as a function of μ is seen to be due to the very great transparency of any elemental material to its own fluorescent x-rays. Thus a more appropriate name would be the "self-transparency" effect. The model shows that if one arranges to have more self absorption by viewing the emitted x-rays at a small angle (3^o) to the sample surface, the response is considerably linearised, but at a great sacrifice of counting rate (figure 10).

In the course of the modelling, calculations have been made down to glancing angles of 1^o. The lower limit to the glancing angle is, of course, set by the approach to the angle of total external reflection at which point the reflection coefficient becomes high and strongly energy dependent. Most materials have a critical angle in the region of 0.5^o. Since the reflection coefficient is an extremely steep function of the angle in this region, maintaining a glancing angle of $>1^o$ will avoid significant effects from energy-dependent variations of the reflection coefficient.

Acknowledgements

I am grateful to my colleagues at Daresbury Laboratory: A.D. Smith for helpful discussions and R.C. Farrow for the rhodium transmission data presented in figure 9.

References

1. X-ray Absorption. Principles, Applications, Techniques of EXAFS, SEXAFS and XANES (Chemical Analysis, Vol. **92**) (Wiley, New York, 1988)

2. J. Jaklevic, J.A. Kirby, M.P. Klein, A.S. Robertson, G.S. Brown and P. Eisenberger, Solid State Communications, **23** 697 (1997)

3. J. Stohr, L.I. Johansson, S. Brennan, M. Hecht and J.N. Miller, Phys. Rev. B **22** 4052 (180)

4. L. Troger, D. Arvanitis, K. Baberschke, H. Michaelis, U. Grimm and E. Zschech, Phys. Rev. B **46** (1992) 3283

5. J. Goulon, C. Goulon-Ginet, R. Cortes and J.M. Dubois, J. Phys. Paris **43** (1982) 539

6. T.M. Hayes and J.B. Boyce, Solid State Phys. **37** (1982) 173

7. T. Rayment, S.L.M. Schroeder, R.M. Lambert, G.D.Moggridge, J.E.Bateman, G.E. Derbyshire and R. Stephenson, "Auger electron detection at ambient pressures for x-ray absorption spectroscopy", unpublished.

8. W.H. McMaster, N. Kerr Del Grande, J.H. Mallett, J.H. Hubbell, UCRL 50174 Sec. II

9. J.E. Bateman, A new model for electron ranges in solid materials, Rutherford Appleton Laboratory report, RAL-TR-2000-051 (http://www-dienst.rl.ac.uk/library/tr/raltr-2000051.pdf)

10. S.L.M. Schroeder, Solid State Communications, **98** (1996) 405

11. T. Tabata, R. Ito and S. Okabe, Nucl. Instr. & Meth. **103** 85 (1972)

12. R. Nakajima, J. Stohr and Y.U. Idzerda, Phys. Rev. B **59** (1999) 6421

Figure Captions

1. A schematic diagram of the interaction of an x-ray beam with a surface at glancing angle ϕ, and the escape of the fluorescent x-rays and electrons.

2. A plot of the functions derived for the escape efficiency of x-rays $\varepsilon_f(w)$ and $\varepsilon_A(u)$ from semi-infinite samples as a function of their respective dimensionless variables $w = \mu\lambda_f/\sin\phi$ and $u = \mu R/\sin\phi$.

3. A plot of the escape efficiency of fluorescent x-rays from a thin layer of thickness d as a function of w. $b = \mu d/\sin\phi$ is the parameter for the various curves.

4. A plot of the escape efficiency of fluorescent x-rays from a thin layer of thickness *d* as a function of *b*. *w* is the parameter for the various curves.

5. A plot of the escape efficiency of fluorescent electrons (augers or photoelectrons) from a thin layer of thickness d as a function of *u*. *d/R* (the layer thickness as a fraction of the electron range) is the parameter for the various curves.

6. A plot of the electron escape efficiency from a thin layer of thickness d relative to that of a semi-infinite sample for the region of u in which the escape efficiency is linear with μ (u<0.2). The form of the fitted function derives from equation (9) approximated under the condition u<<1.

7. A plot for solid elements up to Z=50 of the linear x-ray attenuation coefficients at the K absorption edge ($\lambda=1/\mu$) and the K_α fluorescent line energy (λ_f) [8]. The extrapolated range of the KLL auger electron (R) is also plotted [11]. For elements with Z<10 the density of the solid is set to unity to approximate organic materials.

8. A plot of the key dimensionless parameters $\mu\lambda_f$ and μR for the solid elements up to Z=50.

9. The x-ray surface EXAFS plot predicted by the model as compared with the transmission plot for a rhodium sample. The absorption edges are peak normalised for comparison.

10. The photoelectron interference EXAFS signal (N_{PE}) as a function of the difference between the beam energy (E_B) and the energy of the x-ray absorption edge under study (E_E). It is expressed as a fraction of the auger signal (N_A).

11. The universal curve for the escape efficiency per steradian for x-rays from a semi-infinite sample with the polar angle of the detector's line of sight relative to the normal to the sample as parameter.

12. The multipliers predicted by the model for the relative statistical error in the measurement of μ in a fixed number of incident beam x-rays (N_0T). The two curves present the x-ray and electron cases, assuming that both are counted with 100% efficiency.

13. The multipliers predicted by the model for the relative statistical error in the measurement of μ in a fixed number of detected x-rays or electrons (NT). The two curves present the x-ray and electron cases.

14. The electron energy spectrum (as detected in a GMSD) predicted by the Monte Carlo version of the model in the case of irradiation of a nickel sample at the K shell edge.

15. The source depth profile of the KLL auger electrons predicted by the Monte Carlo version of the model. In the different curves the lower level discriminator on the energy spectrum is varied from zero up to 80% of the KLL auger energy.

16. A comparison of the source depth profile predicted for the nickel KLL auger electrons for the cases of selection of the top 20% and the bottom 20% of the energy spectrum.

17. The simulated x-ray energy spectra expected in a GMSD when a 4nm layer of zinc on top of an iron substrate is irradiated at a 1^{o} glancing angle, just above the zinc K edge.

18. The electron energy spectrum predicted in a GMSD by the model under the same experimental conditions as hold in figure 16.

FIGURE 1

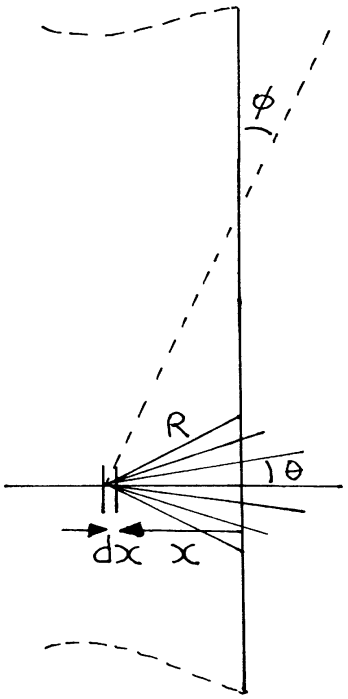

FIGURE 2

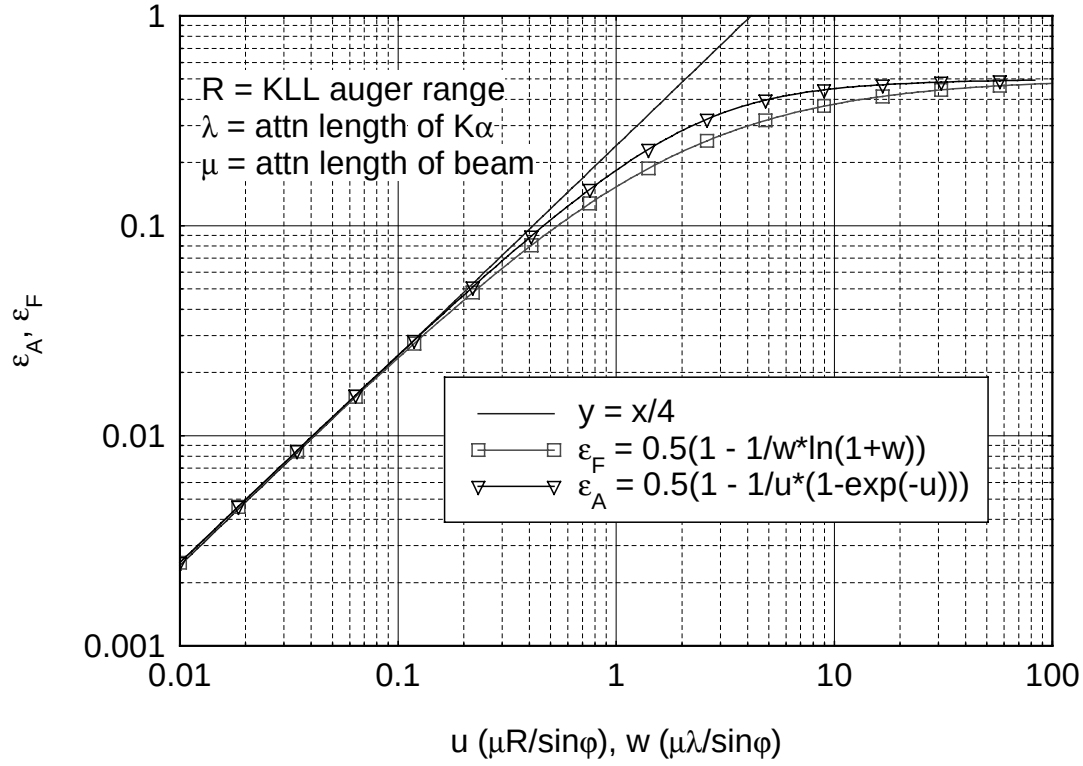

FIGURE 3

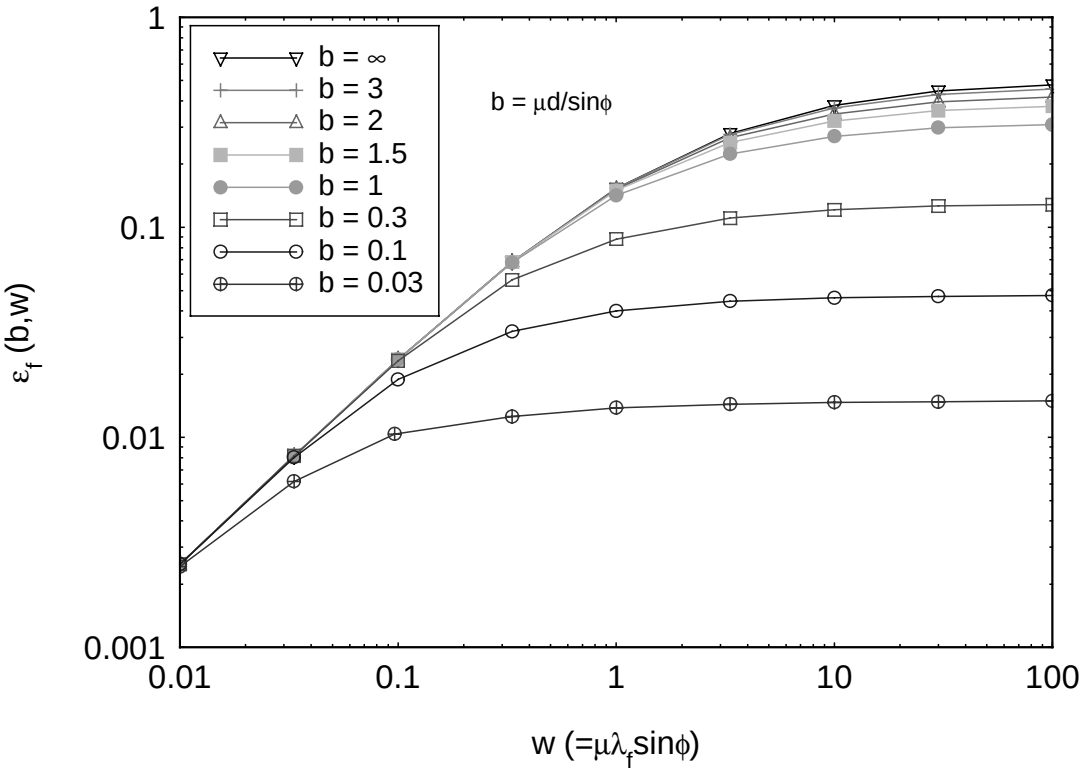

FIGURE 4

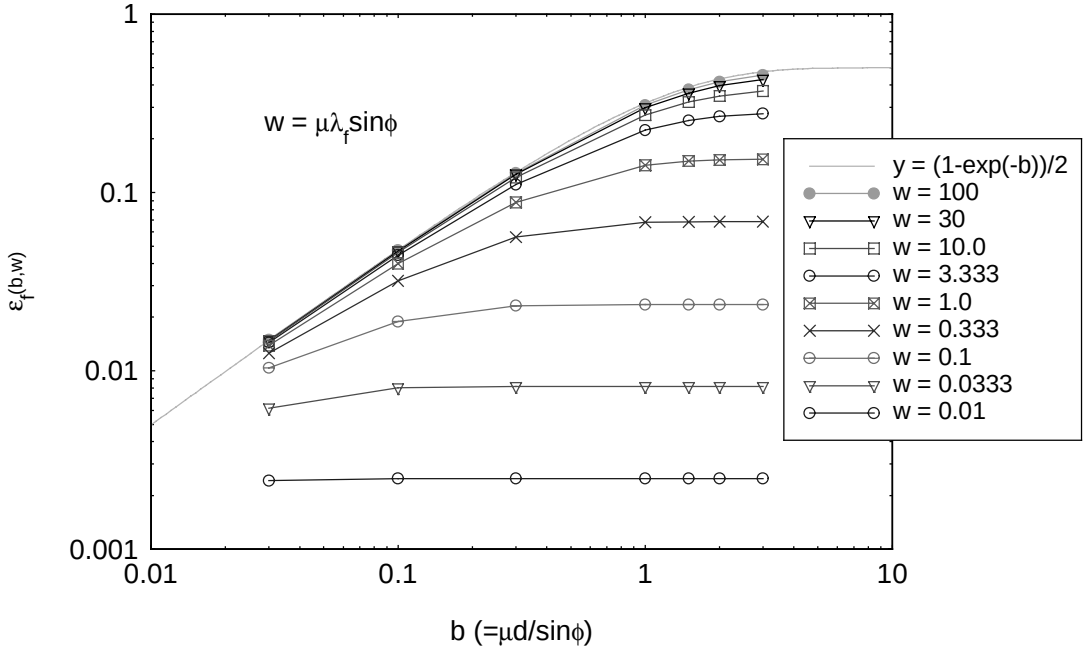

FIGURE 5

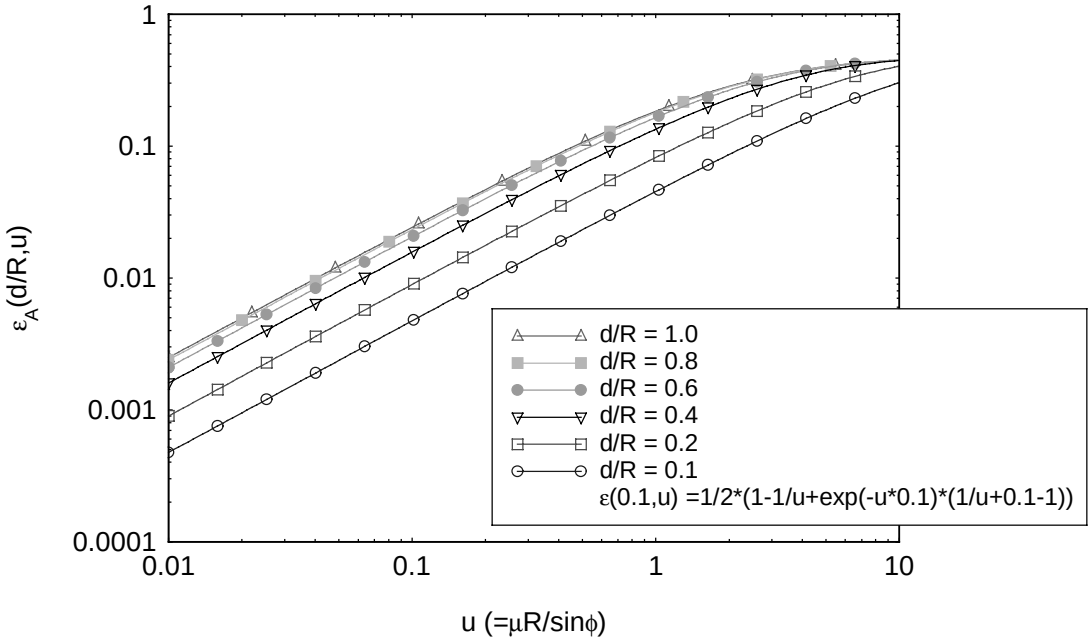

FIGURE 6

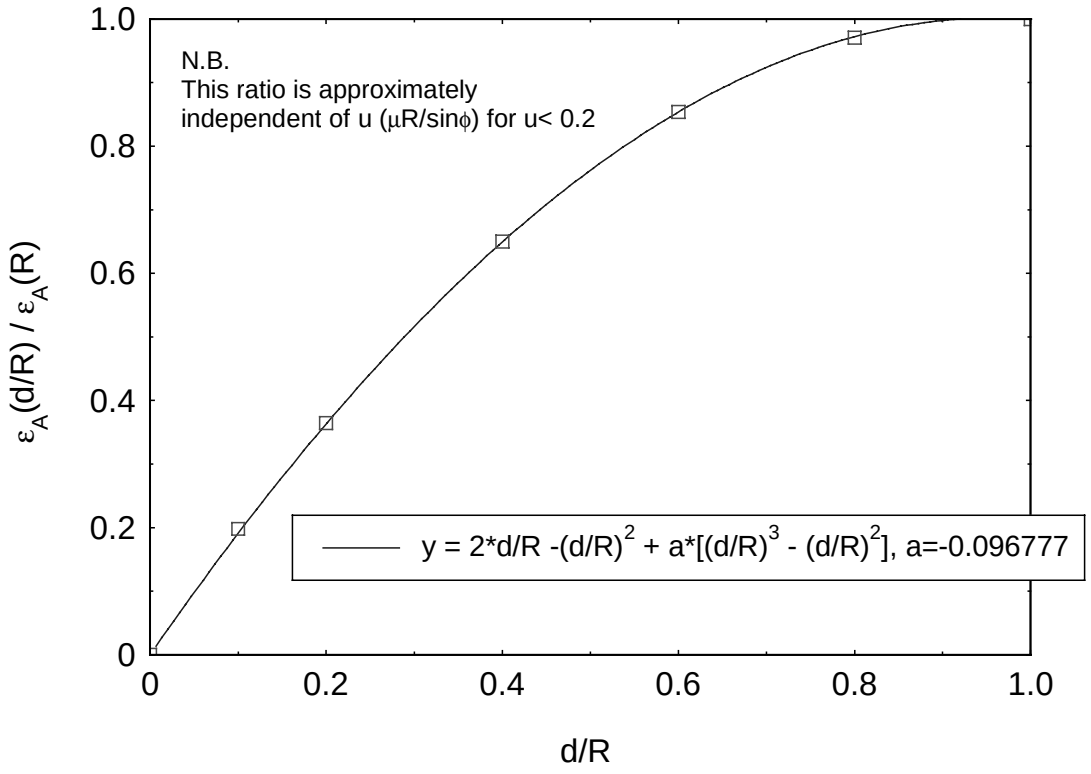

FIGURE 7

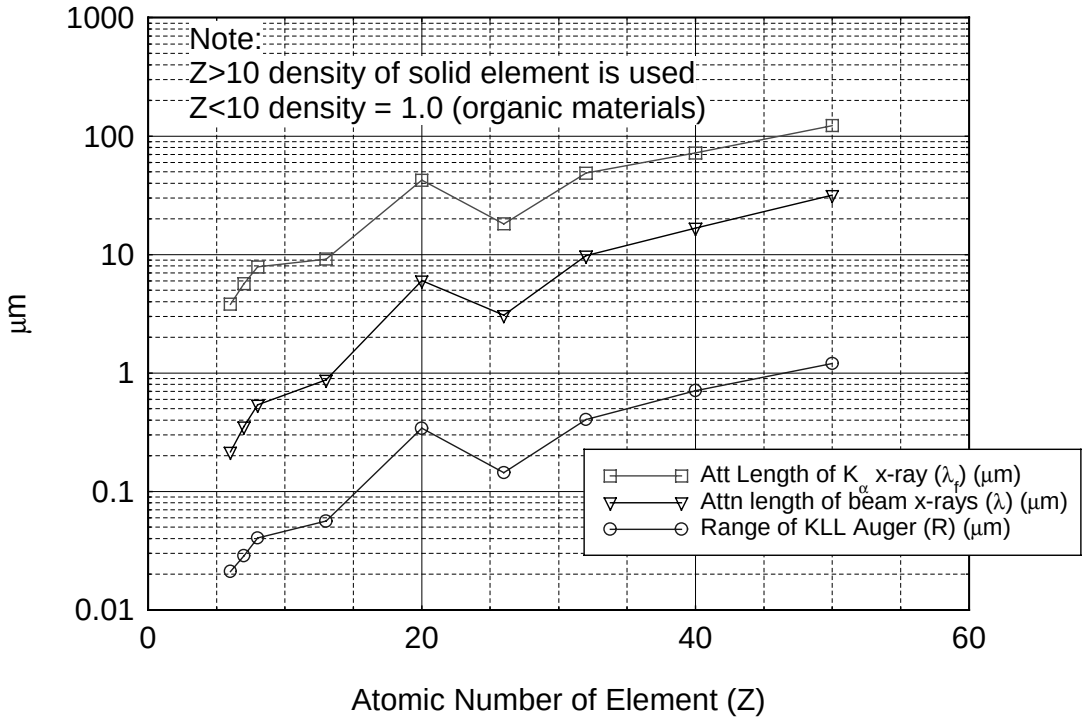

FIGURE 8

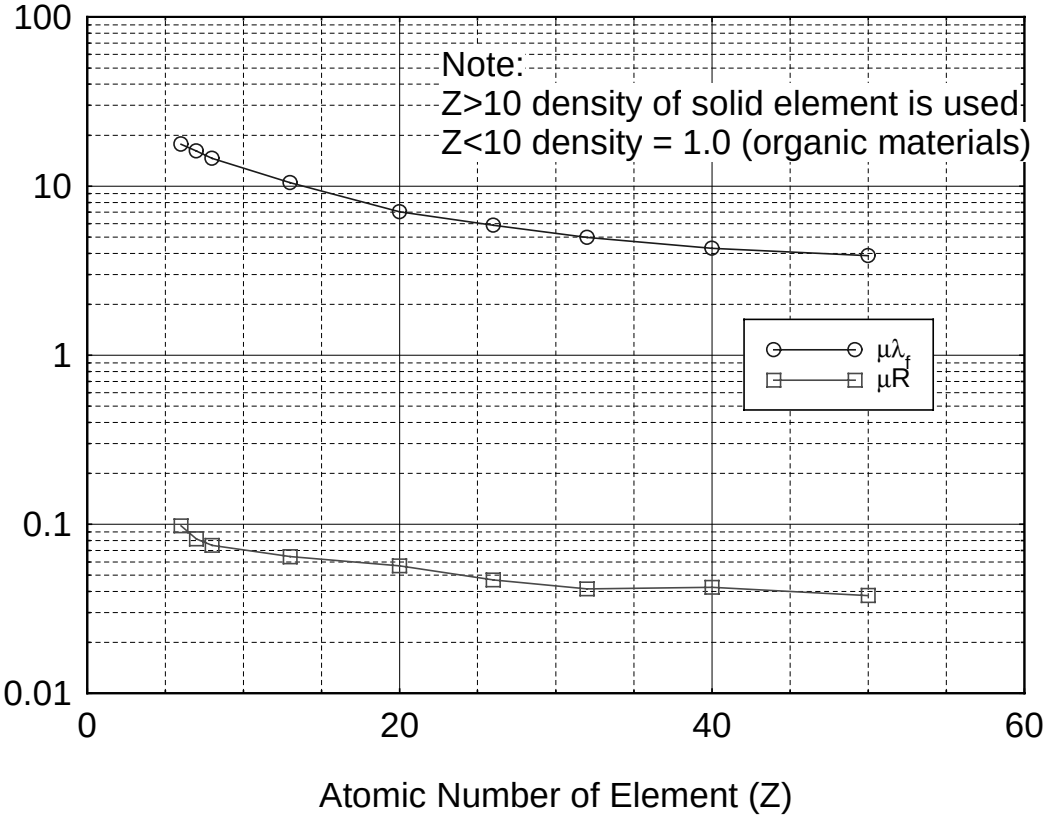

FIGURE 9

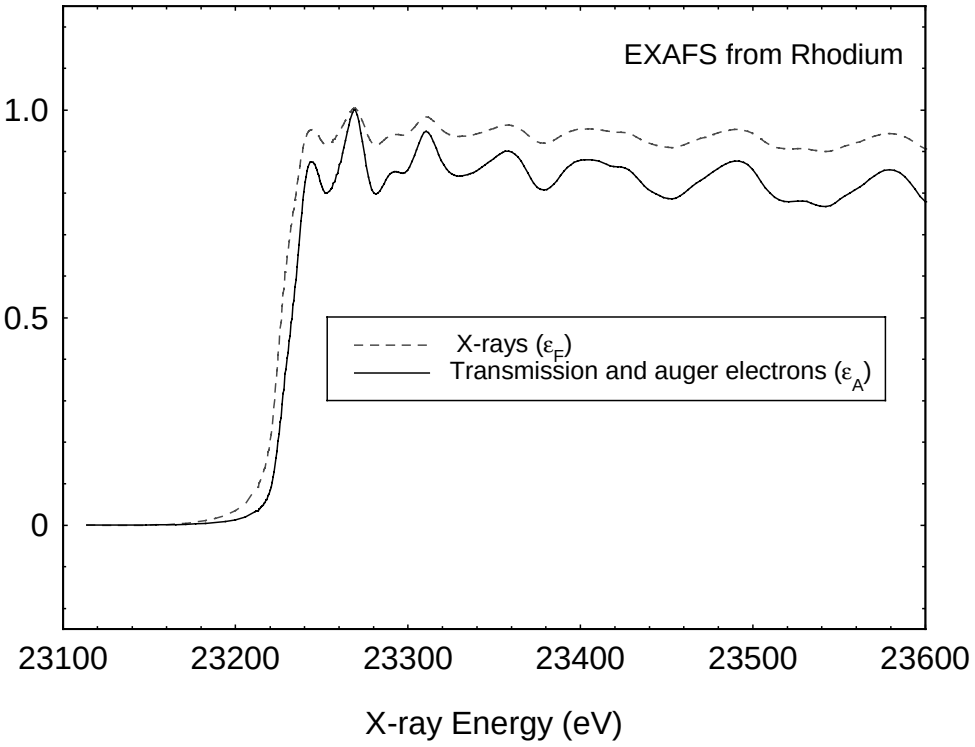

FIGURE 10

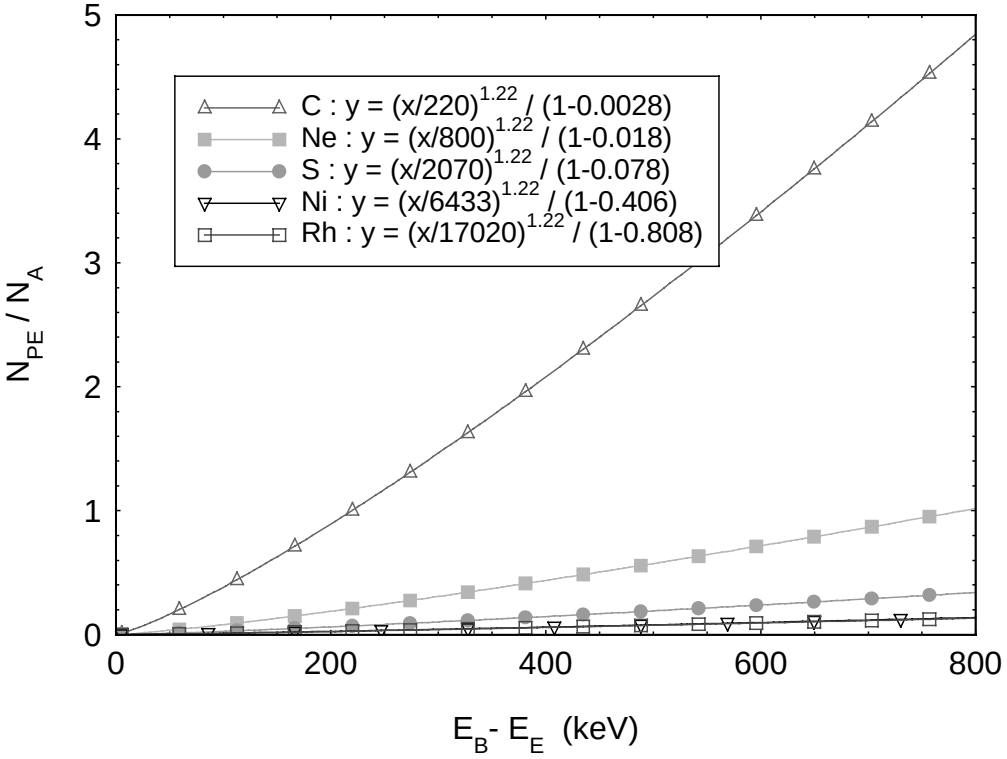

FIGURE 11

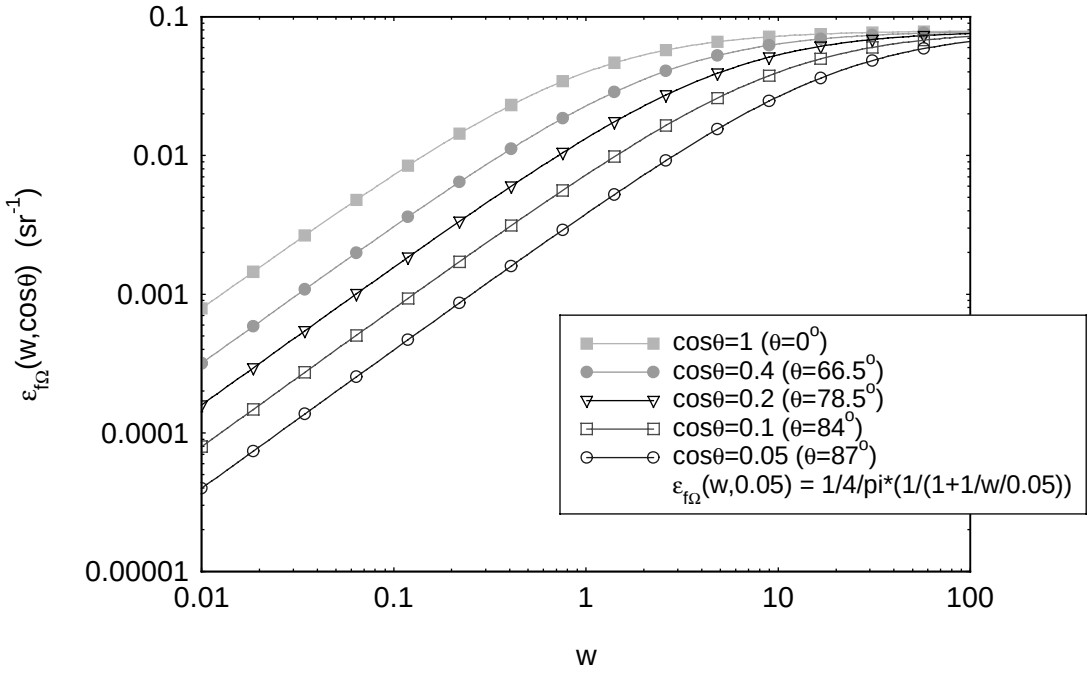

FIGURE 12

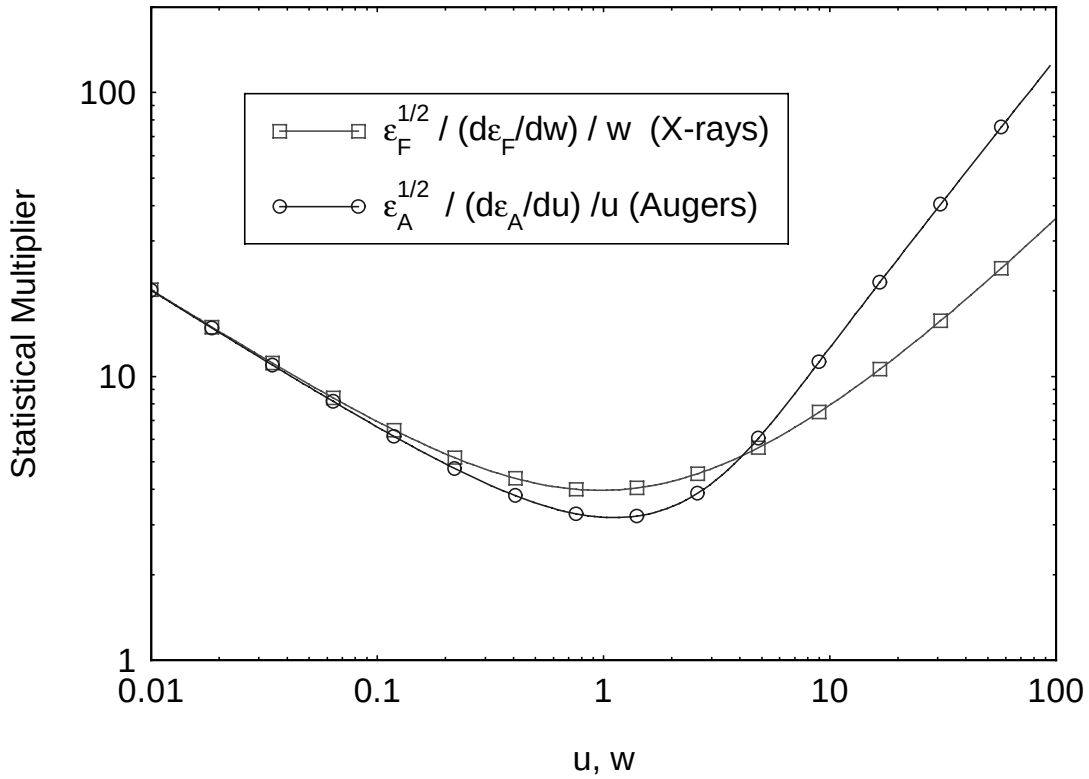

FIGURE 13

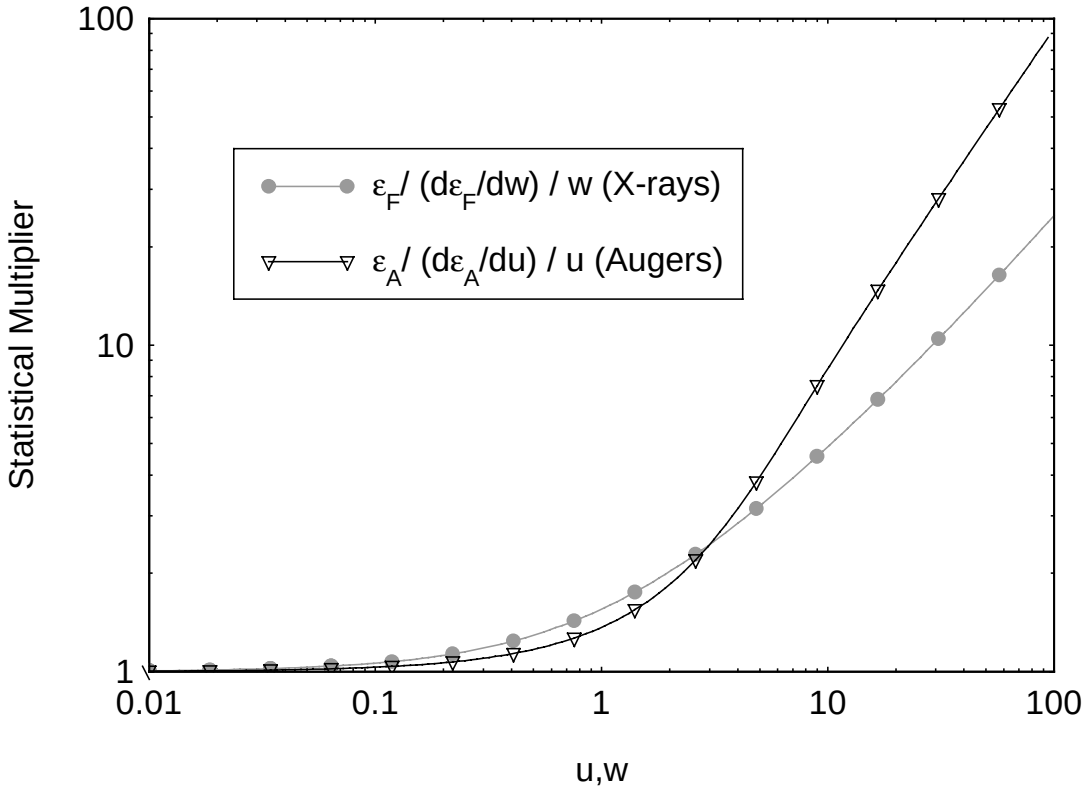

FIGURE 14

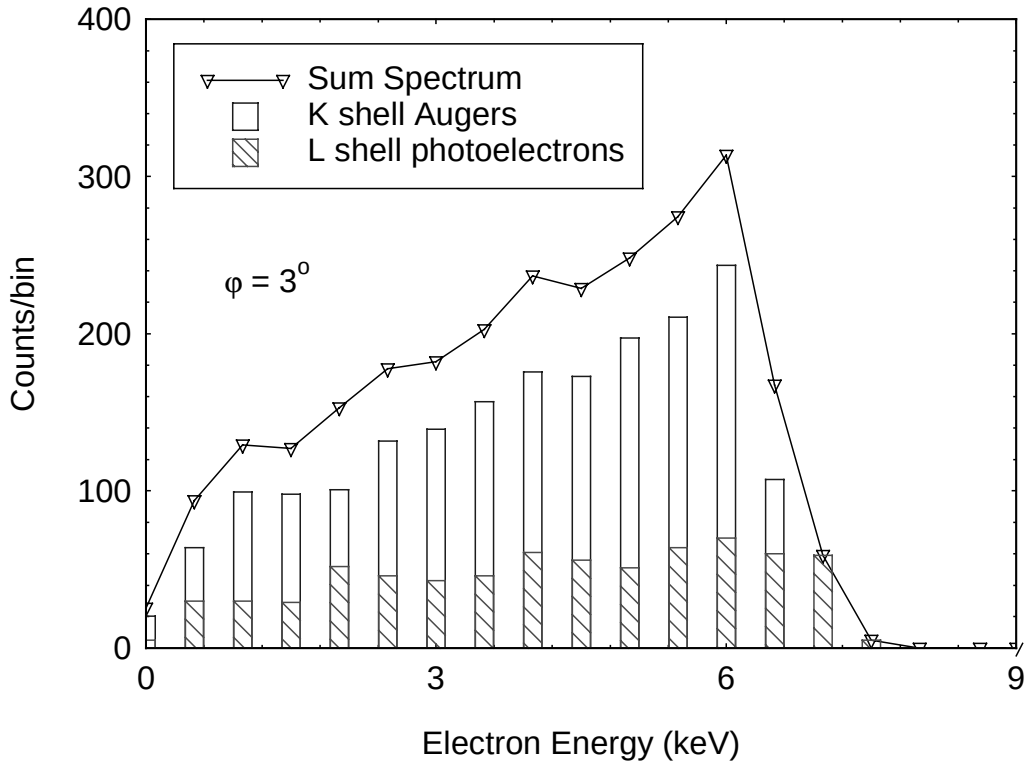

FIGURE 15

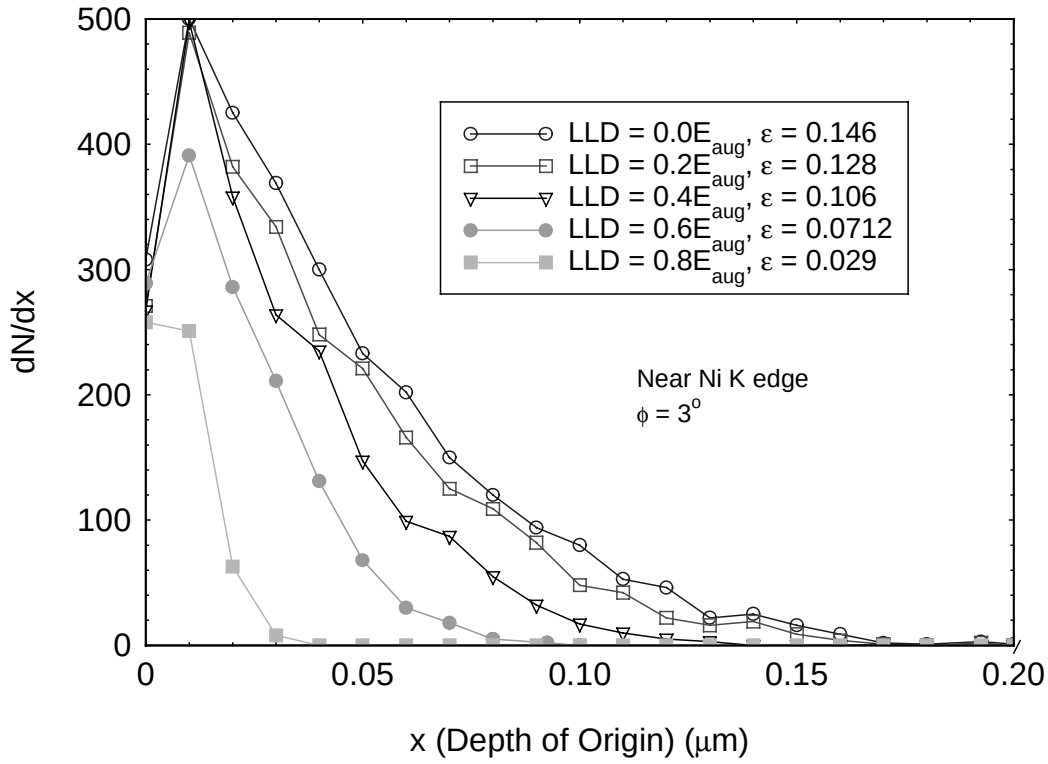

FIGURE 16

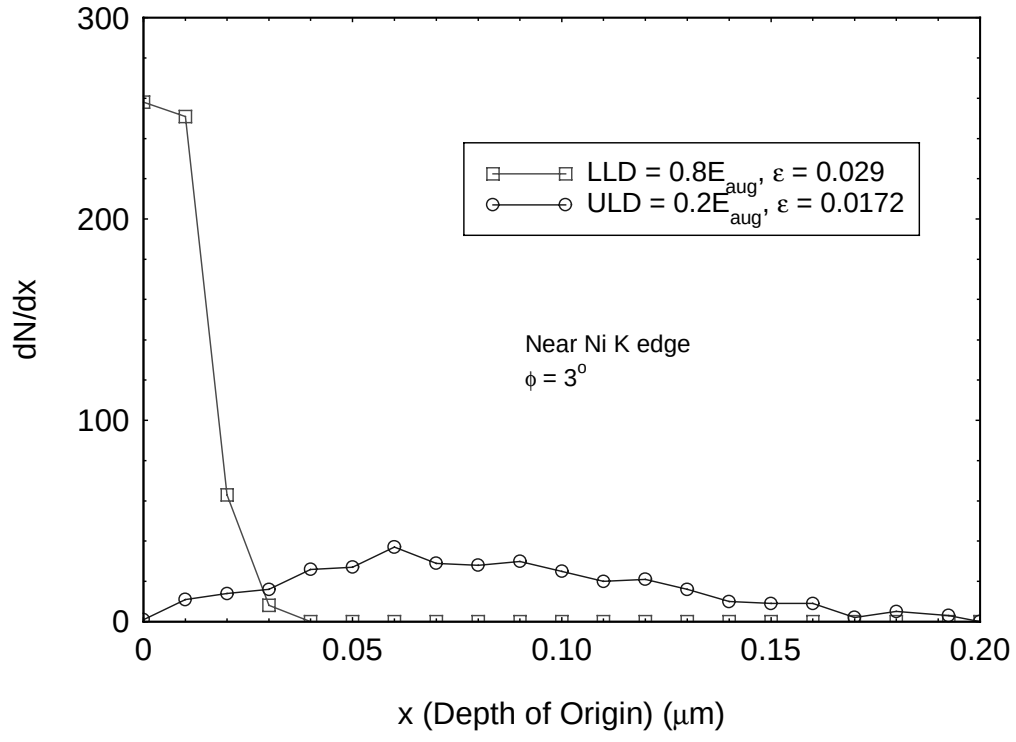

FIGURE 17

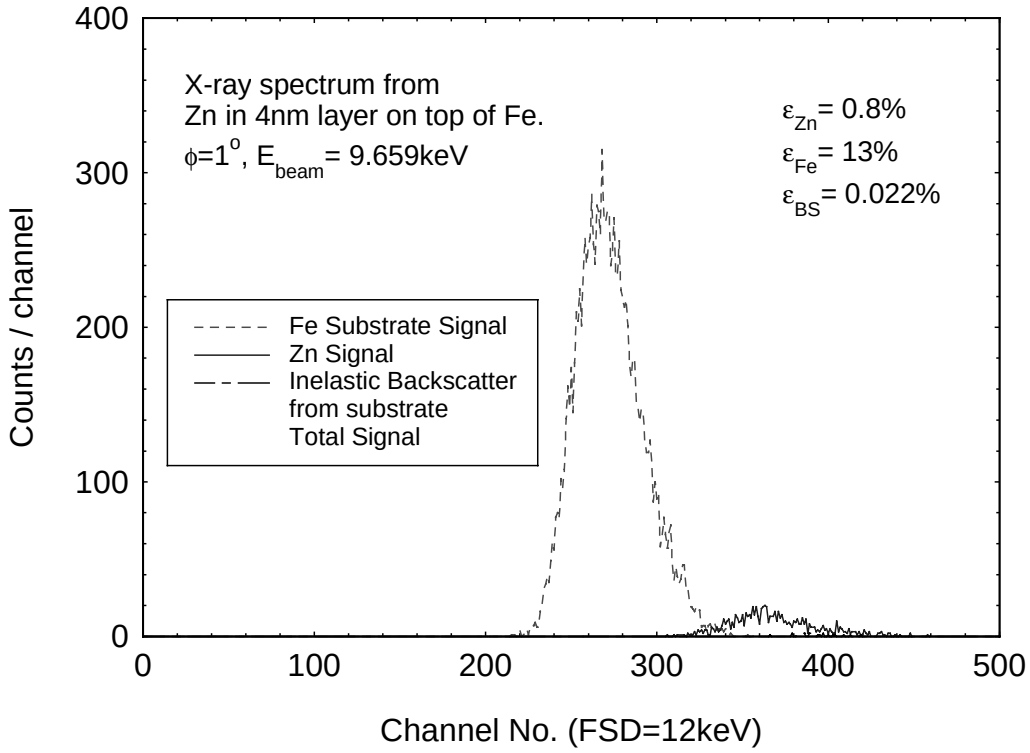

FIGURE 18